The Astronomical Journal, 161:254 (17pp), 2021 June https://doi.org/10.3847/1538-3881/abefdc

The APOGEE Data Release 16 Spectral Line List

Verne V. Smith[1], Dmitry Bizyaev[2,3], Katia Cunha[4,5], Matthew D. Shetrone[6], Diogo Souto[7], Carlos Allende Prieto[8,9], Thomas Masseron[8,9], Szabolcs Mészáros[10,11], Henrik Jönsson[12,13], Sten Hasselquist[14], Yeisson Osorio[15,16], D. A. García-Hernández[8,9], Bertrand Plez[17], Rachael L. Beaton[18], Jon Holtzman[19], Steven R. Majewski[20], Guy S. Stringfellow[21], and Jennifer Sobeck[22]

[1] NSF's NOIRLab, 950 N. Cherry Ave. Tucson, AZ 85719, USA; vsmith@noao.edu
[2] Apache Point Observatory and New Mexico State University, Sunspot, NM 88349, USA
[3] Sternberg Astronomical Institute, Moscow State University, Moscow, 119992, Russia
[4] Steward Observatory, Department of Astronomy University of Arizona, Tucson, AZ 85721, USA
[5] Observatório Nacional, MCTI, Rio de Janeiro, Brazil
[6] McDonald Observatory and Department of Astronomy University of Texas, Austin, TX 78712, USA
[7] Universidade Federal de Sergipe, Brazil
[8] Instituto de Astrofísica de Canarias (IAC), E-38205 La Laguna, Tenerife, Spain
[9] Universidad de La Laguna (ULL), Departamento de Astrofísica, E-38206 La Laguna, Tenerife, Spain
[10] ELTE Eötvös Loránd University, Gothard Astrophysical Observatory, 9700 Szombathely, Szent Imre H. st. 112, Hungary
[11] MTA-ELTE Exoplanet Research Group, Hungary
[12] Materials Science and Applied Mathematics, Malmö University, SE-205 06 Malmö, Sweden
[13] Lund Observatory, Department of Astronomy and Theoretical Physics, Lund University, Box 43, SE-22100 Lund, Sweden
[14] Department of Physics & Astronomy, University of Utah, Salt Lake City, UT 84112, USA
[15] Instituto de Astrofísica de Canarias (IAC), E-38205 La Laguna, Tenerife, Spain
[16] Universidad de La Laguna (ULL), Departamento de Astrofísica, E-38206 La Laguna, Tenerife, Spain
[17] LUPM, UMR 5299, Universite de Montpellier, CNRS, 34095 Montpellier, France
[18] Department of Astrophysical Sciences, Princeton University, 4 Ivy Lane, Princeton, NJ 08544, USA
[19] Astronomy Department, New Mexico State University, Las Cruces, NM 88003, USA
[20] Department of Astronomy, University of Virginia, P.O. Box 400325, Charlottesville, VA 22904, USA
[21] Center for Astrophysics and Space Astronomy, Department of Astrophysical and Planetary Sciences, University of Colorado, Boulder, CO 80309, USA
[22] Department of Astronomy, Box 351580, University of Washington, Seattle, WA 98195, USA
Received 2021 January 14; revised 2021 March 5; accepted 2021 March 9; published 2021 May 5

Abstract

The updated *H*-band spectral-line list (from λ15000–17000) adopted by the Apache Point Observatory Galactic Evolution Experiment (APOGEE) for the SDSS-IV Data Release 16 (DR16) is presented in this work. The APOGEE line list is a combination of atomic and molecular lines, with data drawn from laboratory, theoretical, and astrophysical sources. Oscillator strengths and damping constants are adjusted using high signal-to-noise, high-resolution spectra of the Sun, and α Boo (Arcturus), as "standard stars." Updates to the DR16 line list, as compared to the previous DR14 version, include the addition of molecular H_2O and FeH lines, as well as a much larger (by a factor of $\sim$4) atomic line list, including a significantly greater number of transitions with hyperfine splitting. More recent references and line lists for the crucial molecules, CO and OH, as well as for C_2 and SiH, are also included. In contrast to DR14, DR16 contains measurable lines from the heavy neutron-capture elements cerium (as Ce II), neodymium (as Nd II), and ytterbium (as Yb II), as well as one line from rubidium (as Rb I), which may be detectable in a small fraction of APOGEE red giants.

Unified Astronomy Thesaurus concepts: High-resolution spectroscopy (2096); Atomic spectroscopy (2099); Molecular spectroscopy (2095); Spectroscopy (1558)

Supporting material: machine-readable table

1. Introduction

The Apache Point Observatory Galactic Evolution Experiment (APOGEE; Majewski et al. 2017) is one program under the aegis of the Sloan Digital Sky Surveys (SDSS), as part of SDSS-III (Eisenstein et al. 2011) and SDSS-IV (as APOGEE-2; Blanton et al. 2017). APOGEE[23] is a large spectroscopic survey, expected to exceed $\sim$700,000 stars; these consist primarily of Galactic red giants from all stellar populations, but also include the Magellanic Clouds, and other nearby dwarf galaxy red giants, as well as significant numbers of cool (FGKM) dwarf stars (Zasowski et al. 2013, 2017). The data from APOGEE consist of high-resolution ($R \sim 22{,}500$), near-infrared (NIR) spectra, covering the wavelength range λ1.51–1.70 μm; the spectra are obtained from two 300-object, fiber-fed spectrographs (Wilson et al. 2019), one in the north, mated to the SDSS 2.5 m telescope (Gunn et al. 2006) at Apache Point Observatory (APO), with the added capacity to collect some spectra via a second fiber-feed to the New Mexico State University's 1 m telescope (Holtzman et al. 2010), together with a second spectrograph in the South, on the du Pont 2.5 m telescope (Bowen & Vaughan 1973) at Las Campanas Observatory (LCO).

The data are reduced to sky-subtracted, one-dimensional spectra via the pipeline described in Nidever et al. (2015). Fundamental stellar parameters (effective temperature, $T_{\rm eff}$, surface gravity, $\log g$, and overall metallicity, [M/H]), as well as detailed chemical abundances, are derived from the stellar spectra using the APOGEE Stellar Parameter and Chemical Abundance Pipeline (ASPCAP; García Pérez et al. 2016).

[23] In this paper we will refer to APOGEE and APOGEE-2, collectively, as "APOGEE."

ASPCAP finds the best matches between the observed spectra and an extensive library of synthetic spectra; these model spectra are generated using a detailed spectral-line list. New APOGEE results are included in the recent SDSS data release, DR16 (Ahumada et al. 2019), with Jönsson et al. (2020) providing a detailed overview, description, and discussion of the DR16 APOGEE results. As part of DR16, the APOGEE team carried out a significant update to the line list used in the previous release, DR14, described in Shetrone et al. (2015). The updates to the DR16 APOGEE line list are presented and described here.

2. Line List Data Sources

The APOGEE line list consists of both atomic and molecular lines; this section describes the sources and references for the spectral lines comprising the DR16 line list, which were used to compute the stellar spectral libraries. When discussing the transition oscillator strength, f, the product of the transition statistical weight, g, will typically be quoted as well, usually as the value, $\log(gf)$. The APOGEE line list is restricted to a wavelength range of λ15000–17000, only slightly larger than the wavelengths covered by the APOGEE detectors.

2.1. Atomic Lines

A base atomic line list was created using a recent Kurucz (2017) line list from http://kurucz.harvard.edu/linelists/gfnew/gfallwn08oct17.dat, which includes large numbers of transitions split by hyperfine splitting (hfs). The previous APOGEE line list from DR14 used, as a starting point, an earlier version of a Kurucz list, containing a smaller number of lines, by about a factor of four. Figure 1 illustrates the differences in the number of atomic lines from the DR14 list (bottom panel) as compared to the DR16 list (top panel), where the number of lines is shown for each element (plotted as atomic number, Z). The large increase in the number of spectral lines for all elements is apparent, with particularly large numbers of hyperfine-split line components for V and Co included in the new list. There are also a significant number of new heavy-element lines, from Sr to Pd ($Z = 38$–46), in the DR16 list. The DR16 line list also contains a few heavy elements that were not included in the DR14 list, including Ce II (from Cunha et al. 2017), Nd II (from Hasselquist et al. 2016), and Yb II (discussed here).

It should be noted, however, that the atomic line list for APOGEE contains many more lines than are typically detectable in the H-band stellar spectra of cool giants, which are the main targets of the APOGEE survey, or, for example, M-dwarfs, which have also become a significant component of APOGEE; all lines in the Kurucz (2017) line list have been retained in the APOGEE line list, as these may aid future investigations of, for example, very hot stars and nebular features, or help guide future laboratory efforts. Literature and web sources for the all-important gf-values were also reviewed and updated as needed; these are discussed in the next section.

2.1.1. Oscillator Strengths

The APOGEE abundance pipeline, ASPCAP, uses predefined spectral windows to fit synthetic and model spectra, and to derive the chemical abundances of the elements. A list of the selected windows for each element analyzed by the ASPCAP pipeline can be found in the DR16 reference paper by Jönsson et al. (2020). We searched for updates in the gf-values for all atomic transitions in all windows of a given element. It should be kept in mind, however, that in many instances, due to blends with other molecular features, only some pixels spanning an atomic line carry the required fitting information to derive the abundance of a particular species. The first step here was to compile a list of the transitions that were present in the spectral windows used by ASPCAP in the determination of the different elemental abundances. With such a list in hand, we searched the National Institute of Standards and Technology Database (NIST; https://nist.gov/pml/atomic-spectroscopy-databases; Kramida et al. 2017), the Vienna Atomic Line Database (VALD; http://vald.astro.uu.se; Piskunov et al. 1995; VALD1, and Ryabchikova et al. 2015; VALD3), as well as the literature in general for updated sources relating to the f-values of the transitions for each individual element. The preferred sources for these f-values were experimental laboratory measurements; where these were not available, we used theoretical f-values with well-constrained uncertainties. In the absence of these data, the f-values from the Kurucz (2017) line list were used.

Table 1 contains the considered species, and the adopted sources of the f-value data for the atomic lines that ultimately served as input for the construction of the APOGEE line list. Where an f-value was taken from the NIST database, we note it in the table (along with the original reference); in such cases, we adopt the NIST grading system for assessing uncertainties in the f-values. The NIST grading system, along with the corresponding uncertainty percentages and associated errors in the $\log(gf)$ values, are presented in Table 2. If the f-value was taken from a literature reference, we use the uncertainties quoted in the studies themselves.

The NIST database contained f-values for a number of the element transitions in the APOGEE spectral windows; in most cases these were laboratory measurements, although other references, such as TOPBASE (Opacity Project), as well as theoretical data with well-constrained uncertainties, are also included in the NIST compilation, and are used here. The NIST $\log(gf)$ values for the H I, He I, C II, C III, C IV, N I, N II, N III, N V, O I, O II, O III, Mg II, Si II, and Si III transitions (with no windows in ASPCAP) remained the same as in the previous APOGEE line list (we refer to Table 1 in Shetrone et al. 2015 for the specific references used). For the two Na I transitions ($\lambda_{\rm Air}$=16373.853 Å and 16388.858 Å) in the two sodium windows, the NIST database provides accurate (accuracy="A") $\log(gf)$ values from the NIST "Multiconfiguration Hartree–Fock and Multiconfiguration Dirac–Hartree–Fock" Database (non-orthogonal B-spline Configuration interaction calculations; Froese Fischer, downloaded in 2002). For most of the Mg I transitions, we used the experimental f-values given in Pehlivan Rhodin et al. (2017), or the Opacity Project f-values given in Butler et al. (1993), while for three of the Mg I lines we relied on the Kurucz (2017) line list. With respect to the Al I lines, the f-values are taken from the Opacity Project (Mendoza et al. 1995), although these have different levels of accuracy in the NIST Database. For Si I, most of the f-values are drawn from laboratory measurements by the Lund–Malmö atomic physics group (Pehlivan Rhodin 2018); for a few Si I lines unavailable in Pehlivan Rhodin (2018), we used the TOPBASE gf-values (Nahar & Pradhan 1993), or relied on the Kurucz (2017) line list. For the P I lines, we adopted gf-values from the theoretical work of Biémont et al. (1994), along with an estimated uncertainty in the $\log(gf)$-values of 0.1 dex. For the

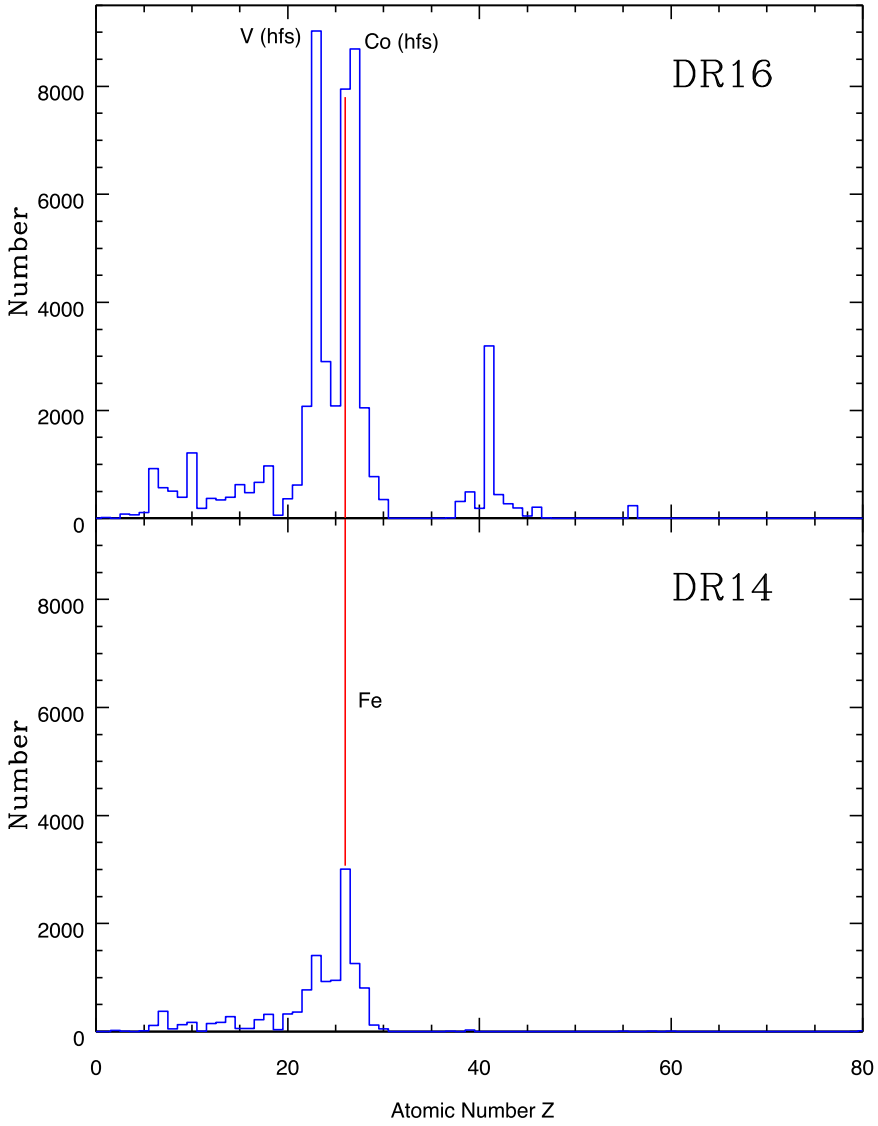

Figure 1. Comparison of the numbers of atomic lines as a function of element (atomic number, Z) for the DR14 base atomic line list (bottom panel) and the DR16 base atomic line list (top panel). The position of Fe ($Z = 26$) is indicated in both panels by a red line. The starting atomic line list for DR16 contains more than 4 × the number of lines from DR14, with a large increase in transitions with hfs, as well as a significant number of new heavy-element ($Z > 30$) lines. The same vertical scale is used for both panels, in order to highlight the increase in numbers of atomic transitions in DR16, as compared to DR14.

S I, K I, and Ca I transitions we used the theoretical studies of Zatsarinny & Bartschat (2006), Safronova et al. (2013), and Hansen et al. (1999), respectively.

Laboratory measurements of oscillator strengths are not available in the APOGEE spectral window for V I, Cr I, Co I, Ni I, or Cu I; we therefore relied on the *gf*-values given in the baseline Kurucz (2017) line list. There are many transitions of Fe I in the APOGEE windows, and, similarly, there are no experimental data available for most of them, apart from several Fe I lines that were specifically studied to cover the APOGEE region in Ruffoni et al. (2013), and a few Fe I lines given in Fuhr & Wiese (2006). For manganese, we adopted the laboratory measurements of Blackwell-Whitehead et al. (2005), where available. For most of the Ti I lines we used the laboratory measurements of Blackwell-Whitehead et al. (2006), and Lawler et al. (2013); for one Ti I transition we used the Kurucz *f*-value. Wood et al. (2014) provided a laboratory *f*-value measurement in support of the APOGEE Survey observations of the only useful line of Ti II in the APOGEE region ($\lambda_{\rm Air} = 15873.84\,\mathring{A}$).

2.1.2. Heavy-element Lines in DR16

One modification to the DR16 line list was the addition of a modest number of heavy-element ($Z \geqslant 57$) lines, identified via a combination of the spectra of Arcturus and/or the Sun, and the FTS spectra of the "standard" cool giants, as well as s-process enriched red giants observed in APOGEE. Three heavy elements were found to be detectable in the APOGEE window, with identified lines from Ce II (8 lines), Nd II (10 lines), and Yb II (1 line). The initial identifications of these lines were facilitated by the compilation of heavy-element spectral lines in a wavelength range of λ10000–40000 by Outred (1978). By and large, these lines are mostly weak, and are usually blended in $R \sim 22{,}500$ stellar spectra (although a few of the Ce II lines can be fairly strong in red giants); however, abundances have been noted in certain populations observed by APOGEE. Cerium and neodymium are primarily

Table 1
Sources for Oscillator Strengths

Species	Source
C I	NIST—Hibbert et al. (1993)
Na I	NIST—Froese Fischer (2002)
Mg I	Pehlivan Rhodin et al. (2017) NIST—Butler et al. (1993), Kurucz (2017)
Al I	NIST—Mendoza et al. (1995)
Si I	Pehlivan Rhodin (2018) NIST—Nahar & Pradhan (1993), Kurucz (2017)
P I	Biémont et al. (1994)
S I	NIST—Zatsarinny & Bartschat (2006), Kurucz (2017)
K I	NIST—Safronova et al. (2013)
Ca I	Hansen et al. (1999)
Ti I	NIST—Blackwell-Whitehead et al. (2006), Lawler et al. (2013), Kurucz (2017)
Ti II	Wood et al. (2014)
V I	Kurucz (2017)
Cr I	Kurucz (2017)
Mn I	Blackwell-Whitehead et al. (2005), Kurucz (2017)
Fe I	NIST—Fuhr & Wiese (2006), Kurucz (2017)
Co I	Kurucz (2017)
Ni I	Kurucz (2017)
Cu I	Kurucz (2017)
Ce II	Cunha et al. (2017)
Nd II	Hasselquist et al. (2016)

Table 2
Oscillator Strength Uncertainties in NIST

Grade	Uncertainty	$\delta \log(gf)$
AAA	$\leqslant$0.3%	$\pm$0.0013
AA	$\leqslant$1%	$\pm$0.0043
A+	$\leqslant$2%	$\pm$0.0086
A	$\leqslant$3%	$\pm$0.0128
B+	$\leqslant$7%	$\pm$0.0294
B	$\leqslant$10%	$\pm$0.0414
C+	$\leqslant$18%	$\pm$0.0719
C	$\leqslant$25%	$\pm$0.0969
D+	$\leqslant$40%	$\pm$0.146
D	$\leqslant$50%	$\pm$0.176
E	>50%	$\pm$0.300

products of neutron captures via the s-process, while ytterbium can be used to probe the r-process (about 68% of solar-system Yb is produced through r-process nucleosynthesis and 32% from the s-process; Burris et al. 2000).

The oscillator strengths for the Ce II and Nd II lines were taken from the APOGEE studies of Cunha et al. (2017), and Hasselquist et al. (2016), respectively, and details of the line identifications and subsequent determinations of *gf*-values are described in detail in these references. Here, we have used the the *f*-value uncertainties quoted in those studies to constrain the astrophysical fitting.

While the identifications and derivation of *gf*-values for the Ce II and Nd II lines were presented in Cunha et al. (2017), and Hasselquist et al. (2016), the details for Yb II are presented here. The Yb II line identified in the APOGEE spectral window is at $\lambda_{\rm Air} = 16498.42\,\mathring{A}$, with an excitation potential of $\chi = 3.017$ eV and was found to be weak, but isolated in the Center-of-Disk (COD) solar spectrum given by Livingston & Wallace (1991) (see the top panel of Figure 2). Ytterbium in the solar system consists of seven stable isotopes, with 71% consisting of five even isotopes, all having nuclear spins of $I = 0$, and two odd isotopes (29%) with I values of 5/2 and 1/2; however, as this Yb II line will always be quite weak, hyperfine and isotopic splitting are not included in modeling this line.

The solar-system abundance of Yb remains somewhat uncertain, as Asplund et al. (2009) lists a photospheric abundance of $A(\rm Yb) = 1.08$, while the corresponding meteoritic abundance is $A(\rm Yb) = 0.91$. The Database of Rare Earths At Mons University (DREAM) lists a value of $\log(gf) = -0.64$ (http://hosting.umons.ac.be/html/agif/databases/dream.html; Biémont et al. 1999), derived from lifetime calculations by Biémont et al. (1998). Uncertainties in the lifetime calculations, as discussed by Biémont et al. (1998), suggest an uncertainty for this *gf*-value of $\sim \pm 0.06$ dex. This *gf*-value yields a solar abundance (see the top panel of Figure 2) of $A(\rm Yb) = 1.03$, falling almost midway between photospheric and meteoritic values; as such, a value of $\log(gf) = -0.64$ is used in the base atomic line list. The Yb II line is quite clean in the Sun, but weak, as shown in the top panel of Figure 2. At the resolution of the APOGEE spectra ($\sim$0.7 Å), test synthetic spectra show that the line depth becomes too small to be of practical use in measuring Yb abundances in solar-type dwarf stars observed as part of APOGEE.

The overall behavior of the Yb II line in different types of red giant is shown in the bottom three panels of Figure 2. As an illustration of the sensitivity of the Yb II line to ytterbium abundance, each panel in Figure 2 includes three synthetic spectra with differing Yb abundances: one with no Yb, a second with a best-fit Yb abundance, and a third that has a Yb abundance larger than the best-fit abundance by +0.2 dex. Arcturus, shown in the second panel, is an example of a mildly metal-poor K2 giant, where the Yb II line is buried within the (7–4)R59 $^{12}C^{16}O$ line. In the case of a well-studied standard star, such as Arcturus, where the carbon and oxygen abundances are well-determined, the (7–4)R59 feature appears too deep, and the addition of a Yb abundance with [Yb/Fe] = +0.07 reproduces this feature well. The internal uncertainty in the [Yb/Fe] ratio is set by uncertainties in the Yb II *gf*-value ($\pm$0.06 dex), together with the uncertainty in the Arcturus Fe-abundance ($\sim \pm 0.05$ dex.), or by $\pm$0.08 dex if the respective uncertainties are added in quadrature. In similar red giants within the APOGEE survey, observed at lower resolution, the determinations of Yb abundances from this single line will be somewhat uncertain; attempts to determine Yb abundances from APOGEE are favored in warmer red giants (where CO absorption is weaker), and metal-poor, low-gravity giants (where both CO formation is weakened by metallicity-squared, and ionized lines are stronger). The third panel in Figure 2 illustrates a red-clump (RC) giant member of the open cluster NGC2420 (RC giants are common APOGEE targets), 2M07382696+2138244, in the Yb II region, with the Yb II line yielding an abundance of [Yb/Fe] = +0.05. In RC giants, CO contamination is less prevalent than in the cooler giants, with a typical uncertainty in the Fe-abundance of about 0.1 dex, resulting in an estimated internal uncertainty of [Yb/Fe] $\sim \pm 0.12$ dex. The bottom panel shows the Yb II line in 2M17334208-2958347, a cool, moderately metal-poor giant, with a Yb II line fit for an abundance of [Yb/Fe] = +0.15 $\pm$ 0.12.

An additional heavy-element abundance appearing in the DR16 results relates to rubidium ($Z = 37$), which is produced

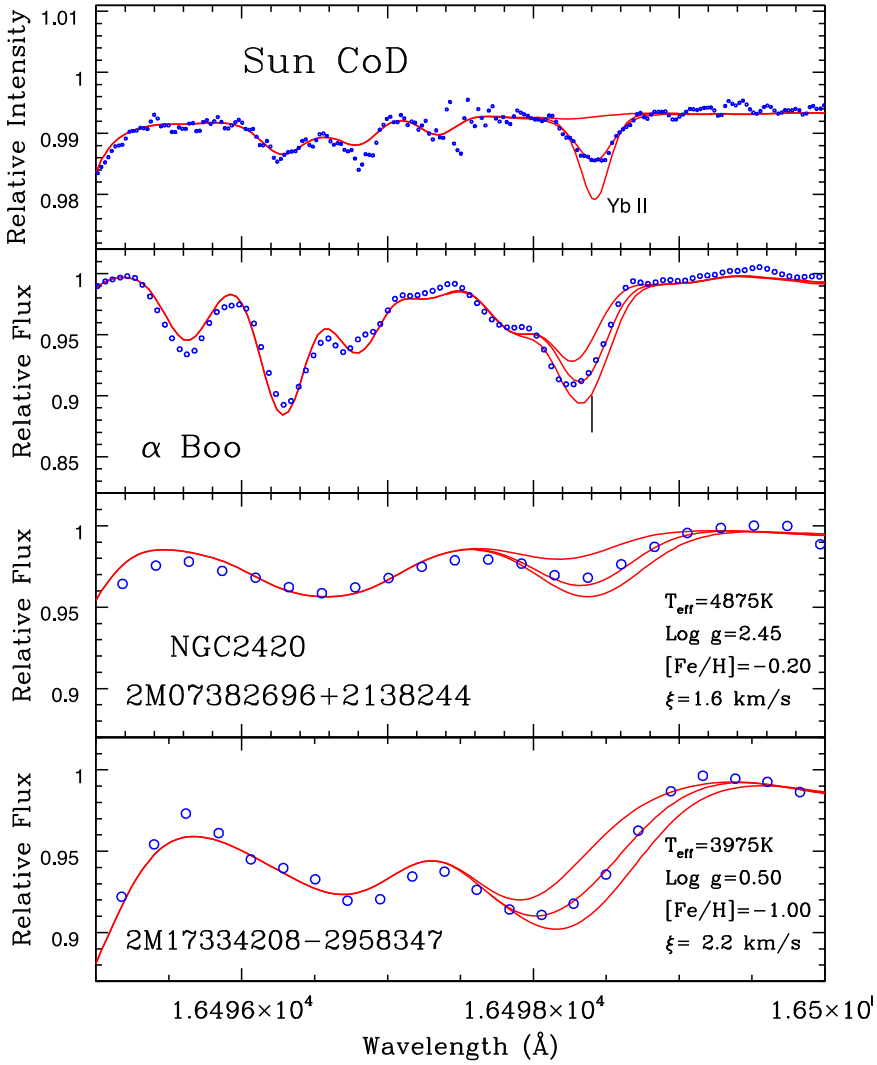

Figure 2. An illustration of the Yb II line (λ16498.42 Å) and its behavior in four different types of stars: the Sun, the mildly metal-poor K-giant Arcturus, a clump giant in the old open cluster NGC 2420, and a moderately metal-poor, cool, field red giant. The solar spectrum is the Center-of-Disk (COD) as given by Livingston & Wallace (1991), the Arcturus spectrum is the FTS atlas of Hinkle et al. (1995), while the bottom two red giant spectra are taken from APOGEE. Each panel contains three synthetic spectra, with one having no Yb, another having a Yb abundance that fits the Yb II line, while a third has a Yb abundance larger by +0.2 dex as compared to the best-fit abundance.

as a result of both r- and s-processes, with the solar-system mixture being 50%/50% (Burris et al. 2000). There is a Rb I doublet in the APOGEE window at air wavelengths of λ15288.430 and λ15289.480, where $\chi = 1.579$ eV (Sansonetti 2008). The wavelengths in the Kurucz line list for these transitions are somewhat different, with air wavelengths of λ15288.938 and λ15289.966, respectively. Tests of the presence of these lines in Arcturus, and in the M-giants β And and δ Oph, indicate that the Sansonetti (2008) wavelengths are preferred, although only the stronger Rb I line at λ15289.480 is detected. This line is weak, but may be detectable in APOGEE spectra of s-process-rich populations, or in the cooler red giants. In addition, non-LTE departure coefficients for these Rb I transitions have been calculated by Korotin (2020).

2.2. Molecular Lines

Molecules in the DR16 list include CO, OH, CN, C_2, H_2O, FeH, and SiH, with the data source for each molecule discussed below, and listed in Table 3.

Table 3
Molecular Line Lists

Molecule	Source
CO	Li et al. (2015)
OH	Brooke et al. (2016)
CN	Sneden et al. (2014)
H_2O	Barber et al. (2006)
C_2	Yurchenko et al. (2018b)
FeH	Hargreaves et al. (2010)
SiH	Yurchenko et al. (2018a)

2.2.1. CO

Rovibrational lines of CO constitute the primary carbon-abundance indicators in the APOGEE red giants (with C/O ⩽ 1) and cool dwarfs, with a number of vibration–rotation band systems running across the APOGEE spectral window, the strongest of which have $\Delta\nu = 3$. The previous DR14 line list used CO data from Goorvitch (1994), whereas in DR16, the CO data have been updated using wavelengths, excitation

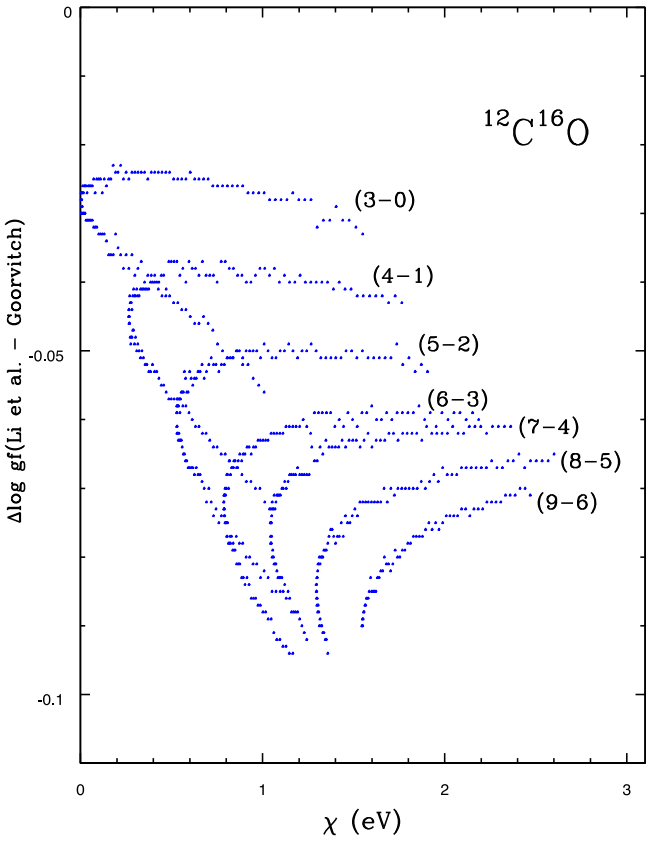

Figure 3. Comparisons of $^{12}C^{16}O$ *gf*-values between Li et al. (2015) and Goorvitch (1994), represented by $\Delta \log(gf)$ (Li et al.–Goorvitch) as a function of excitation potential (χ). The progression of vibration–rotation bands, from (3-0) to (9-6), which run across the 1.5–1.7 μm, are evident, with the differences becoming greater for the higher vibration–rotation bands.

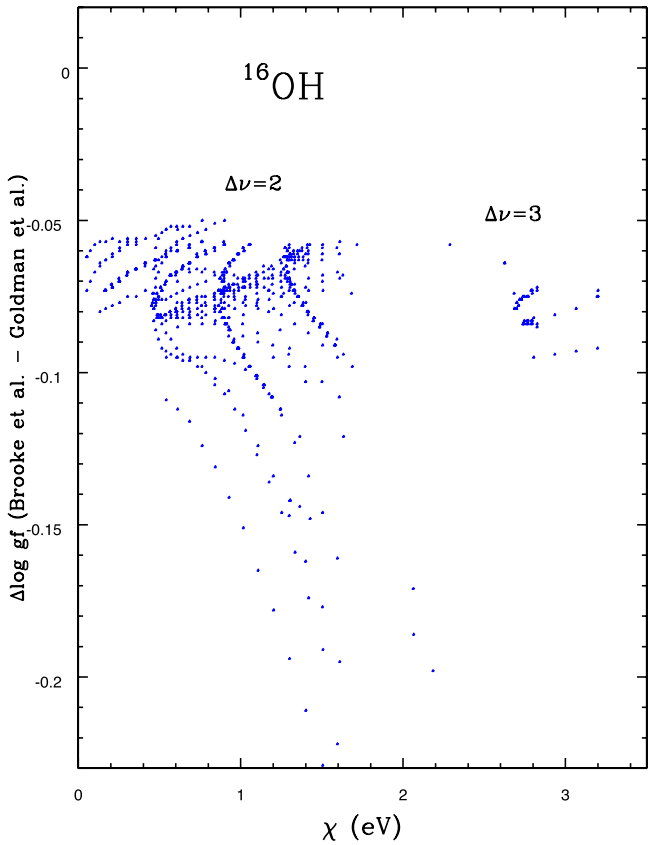

Figure 4. Comparison of Brooke et al. (2015) and Goldman et al. (1998) ^{16}OH *gf*-values for lines falling in the APOGEE window. Absorption from OH is dominated by $\Delta\nu = 2$ transitions, with the structure in the $\log(gf)$ comparisons arising from the (in order of increasing χ) (3–1), (4–2), and (5–3) vibration–rotation systems (the lines at very low χ are (2-0) lines).

potentials, and *gf*-values taken from Li et al. (2015). Due to the importance of CO lines in terms of the derivation of stellar atmospheric parameters, as well as derived carbon abundances, it is useful to compare the CO data of Li et al. (2015) with that of Goorvitch (1994). The energy levels compare very well, with differences below 0.001 eV, while the wavelength differences are typically a few mÅ. There are small, systematic differences in the *gf*-values, and these are illustrated in Figure 3 via $\Delta \log(gf)$(Li et al. - Goorvitch) as a function of excitation potential, χ. Only the detectable CO lines are shown, with $\Delta\nu = 3$; there are higher-level CO lines (with $\Delta\nu \geqslant 4$) that exhibit larger offsets between Li et al. and Goorvitch (of $\sim$+0.3 dex), but these lines have such large excitation potentials that they are too weak to affect the spectra of red giants and cool dwarfs. In the stronger detectable CO lines that represent the major C-abundance indicators, the Li et al. (2015) *gf*-values are slightly smaller than those of Goorvitch (1994), with a mean difference and standard deviation of $\Delta \log(gf)$(Li et al.–Goorvitch)$=-0.06 \pm 0.03$ dex.

In addition to the main CO isotopic combination of $^{12}C^{16}O$, further minor isotopic combinations are also provided in the DR16 line list, including $^{13}C^{16}O$, $^{12}C^{17}O$, and $^{12}C^{18}O$.

2.2.2. OH

As with CO, a number of rovibrational lines from first-overtone bands of OH are found within the APOGEE window; abundances of the critical element oxygen rely on these OH lines. In both the cool red giants and the M-dwarfs, the OH lines are some of the stronger features, remaining detectable down to very low metallicities, and threfore represent useful spectral lines in metal-poor populations.

Spectral-line data for OH were updated for DR16 using Brooke et al. (2016); the DR14 line list used data from Goldman et al. (1998) for OH. A comparison of the *gf*-values between Brooke et al. (2016) and Goldman et al. (1998) is shown in Figure 4, as Δ(log *gf*(Brooke et al.–Goldman et al.)) versus excitation potential, and a systematic shift between the two OH studies can be seen; the Brooke et al. values are slightly smaller, on average, as compared to Goldman et al. (1998), with a mean difference, for the majority of detectable lines, of $\Delta(\log(gf) = -0.08$ dex. This difference becomes greater for higher *J*-values and $\Delta\nu = 3$ s overtone bands; however, these lines become progressively weaker, and do not impact significantly on the derived O-abundances. Minor oxygen isotopes are also included in the OH list (^{17}OH and ^{18}OH).

2.2.3. CN

There is no change in the CN spectral-line source between DR14 and DR16, with the CN data being taken from Sneden et al. (2014). In combination with CO and OH, the CN lines close the constraints on the individual C, O, and N abundances, with these three diatomic molecules providing most of the CNO abundance information.

The minor isotopic lines of $^{13}C^{14}N$ are included in the line list.

2.2.4. C_2

The recent study by Yurchenko et al. (2018b) was the source for the C_2 data, including wavelengths, excitation energies, and *gf*-values. The C_2 lines are, in general, weak in the oxygen-rich red giants constituting the primary targets of APOGEE; however, there are significant numbers of carbon stars in which the C_2 lines are quite strong, and serve as carbon-abundance indicators. The minor isotope, ^{13}C, was included, in both $^{13}C^{12}C$ and $^{13}C^{13}C$ variants.

2.2.5. H_2O

In preparation for DR16, and the inclusion by APOGEE of cooler red giants ($T_{\rm eff} \leqslant 3500$ K), as well as increasing numbers of M-dwarfs, many of which are exoplanet-hosts, H_2O lines were added to the DR16 line list (these were missing from DR14); absorption by numerous water lines becomes increasingly significant in the cooler red giants, as well as in all M-dwarfs.

Data for the H_2O energy levels and Einstein A-values (from which *gf*-values were computed) for the various types of transitions were taken from Barber et al. (2006), and were used to construct the H_2O line list between λ15000 and 17000; within this wavelength interval, the Barber data resulted in the generation of over 26 million water lines (using only one isotopic combination of $^1H_2^{16}O$; deuterated water, and the minor isotopes of ^{17}O and ^{18}O, considered to be insignificant sources of H_2O absorption).

Including this large number of H_2O lines in the spectral synthesis calculations required to generate such a large number of library spectra is impractical, so the H_2O lines were culled to remove the weakest lines. A very large fraction of the water lines are extremely weak, and a so-called "Boltzmann cut" was applied to remove the weakest lines; the relative strength of a spectral line from a particular species depends on the combination of $\log(gf\lambda)$, temperature, and excitation potential, χ, with the relative line strength, S, often written as $S = \log(gf\lambda) - \theta\chi$, where $\theta = 5040/T$, with χ having units of eV and T in Kelvin; here, λ is normalized to 16000 Å. Using an excitation temperature of $T = 3500$ K, two H_2O line lists were prepared, with one containing only transitions with $S > -8.5$, and another with only $S > -9.5$, such that only these stronger H_2O lines were used in calculating the spectral libraries (i.e., the Boltzmann cuts). These particular cuts were performed following tests based on synthetic cool-dwarf spectra, in which spectra computed with and without the cut were compared, and found to differ by less than 1% in flux. The criteria for the inclusion of either the $S > -8.5$ list, or the $S > -9.5$ list, or no inclusion of water lines at all were as follows: (1) if $T_{\rm eff} > 4000$ K, H_2O lines were not included in the library spectra, (2) if $T_{\rm eff} = 3250$–4000 K, or $[M/H]+[\alpha/M] > -1.5$, the $S > -8.5$ line list was used, and (3) if $T_{\rm eff} < 3250$ K, the $S > -9.5$ line list was used. In the end, these culled lists of H_2O lines added to the DR16 line list were found to fit, and match very well, with the H_2O absorption of the M-dwarfs analyzed by Souto et al. (2017, 2018, 2020).

In addition to synthesizing and matching H_2O absorption features in the M-dwarfs as a test of the DR16 line list, transitions generated by the Barber et al. (2006) energy levels can be compared with data for H_2O lines from the more recent study by Polyansky et al. (2018), which appeared after the freezing of the DR16 line list. Polyansky et al. (2018) included higher energy levels, up to a maximum energy of 41,000 cm^{-1} (5.08 eV), while Barber et al. (2006) included energy levels up to an energy level of 30,000 cm^{-1} (3.7 2eV). The inclusion of higher energies in Polyansky et al. (2018) led to a significant increase in the number of H_2O energy levels (810,269) in comparison to the Barber et al. (2006) total of 221,097 levels. This leads to the presence of many more transitions in Polyansky et al. (2018), although the higher-energy transitions are typically either weak or undetectable in the APOGEE targets. Polyansky et al. (2018), in their Figure 2, compare their line list with that of Barber et al. (2006) as a plot of H_2O absorption, calculated for $T_{\rm exc} = 4000$ K, versus wavenumber. This comparison reveals that, in the infrared, the two line lists produce absorptions that are quite similar, including over the APOGEE wavenumber regime ($\sigma = 5880$–6667 cm^{-1}), while at higher wavenumbers, particularly in the optical ($\sigma > 15{,}000$ cm^{-1}), the absorption differences become much larger.

Differences between the Barber et al. (2006) and Polyansky et al. (2018) H_2O line lists across the APOGEE spectral window were investigated using cool stellar atmosphere models and comparing the synthetic spectra, an example of which is shown in Figure 5. This particular example is for a model atmosphere having $T_{\rm eff} = 3500$ K, $\log g = 4.5$, $[Fe/H] = 0.0$, and $\xi = 1.0$ km s^{-1}, while the wavelength interval chosen for the plot is close to that in which H_2O absorption is relatively strong (note, only H_2O lines are included in the synthesis, in order to facilitate a direct comparison). Differences between the two line lists are not large, being typically less than a few percent. Quantitative comparisons to observed M-dwarf APOGEE spectra indicate that the more recent Polyansky et al. (2018) data provide a marginally better fit than the older Barber et al. (2006) data, although the fits are not significantly better. Testing of the H_2O line lists will continue toward the final planned data release (DR17).

2.2.6. FeH

The DR14 APOGEE line list did not include transitions from iron hydride, although FeH is an important contributor to the H-band APOGEE spectra of M-dwarfs (Souto et al. 2017). Spectral lines from FeH were added to DR16 using data from Hargreaves et al. (2010), which consist of lines arising from $E^4\Pi$-$A^4\Pi$ electronic transitions from λ1.58 μm up to λ1.7 μm. Wallace & Hinkle (2001) identified lines from this transition in the spectra of sunspots, along with M and L dwarfs, and these FeH lines closely match the wavelengths of lines in M-dwarf APOGEE spectra that were missing from the DR14 syntheses.

Hargreaves et al. (2010) do not provide *gf*-values for the FeH lines, so Souto et al. (2017) computed *gf*-values using the line intensities provided by Hargreaves et al. (2010), and the expression for converting HITRAN–like intensities to Einstein *A*-values from Šimečková et al. (2006; see their Equation (20)). The *A*-values were then converted to *gf*-values using the standard expression given by Larsson (1983):

$$gf = (1.499(2J + 1)A)/(\sigma^2)$$

where A is the Einstein A-value (in s^{-1}), J is the lower-state angular momentum, and σ is the wavenumber (in cm^{-1}). The *gf*-values presented in Souto et al. (2017) were adopted for the DR16 line list.

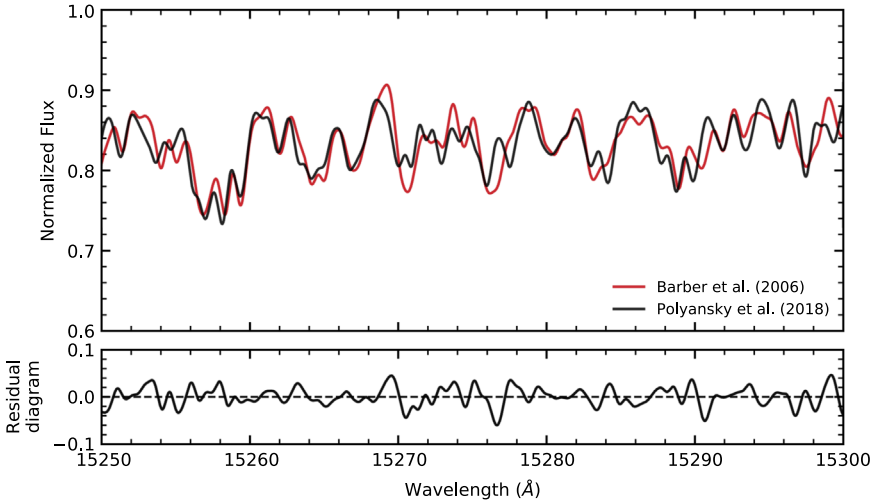

Figure 5. Comparison of an H_2O synthetic spectrum generated using the DR16 Barber et al. (2006) line list (top panel, red line) with one computed from the list given in Polyansky et al. (2018) (black line). Differences, in the sense of Barber−Polyansky, are shown in the bottom panel. There are rather small (∼0%–5%) differences in absorption, as well as slight differences in wavelength, which are not due to differences in *gf*-values for the same transitions (which agree), but to the additional lines from higher excitation energies included in the Polyansky et al. (2018) list. The synthetic spectra were computed with a model atmosphere, having $T_{\rm eff} = 3500$ K, $\log g = 4.5$, and $[{\rm Fe/H}] = 0.00$.

2.2.7. SiH

Although SiH lines are expected to be weak (and undetectable) in virtually all of the APOGEE red giants and dwarfs, these molecular lines were included in the line list. The data were taken from Yurchenko et al. (2018a), and include the isotopes ^{28}SiH, ^{29}SiH, and ^{30}SiH.

2.2.8. Molecular Absorption Comparisons in APOGEE Spectra of a Typical Red Giant and M-Dwarf

As an aid to visualizing the relative importance of various molecules in shaping the absorption-line spectra in cool giants and dwarfs, molecular synthetic spectra are illustrated in Figure 6 for the more significant molecules (OH, CO, CN, H_2O, and FeH), with an isolated spectrum for each molecule. The spectra were computed for models of a typical APOGEE M-giant and M-dwarf. This figure provides a sense of how much each molecular species influences the red giant and red dwarf spectra, respectively.

3. Astrophysical Adjustment to the Line Parameters

As shown previously by Shetrone et al. (2015), the combined list of theoretical and laboratory *gf*-values and damping constants for atomic spectral lines strong enough to be clearly detected and well-sampled can be improved by comparisons with high-resolution, high-quality spectra of well-studied standard stars, i.e., by applying "astrophysical" adjustments. Note that these adjustments are limited to atomic lines only, and that no adjustments were made to the molecular lines discussed in Sections 2.2.1–2.2.7.

3.1. Astrophysical Adjustment Methodology

We follow the approach used by Shetrone et al. (2015): spectral-line parameters are adjusted for well-defined lines in the model spectra of the Sun, and the K-giant Arcturus (α Boo), in order to match the observed lines in high-resolution, high-S/N FTS spectra within the limits of the laboratory (or theoretical) parameter uncertainties.

The line-matching code employed by Shetrone et al. (2015), and described in Bizyaev & Shetrone (2015), was adopted, as were the reference FTS spectra used in previous APOGEE line lists: the center-of-disk (COD) solar spectrum is taken from Livingston & Wallace (1991), and the NIR spectral atlas of Arcturus from Hinkle et al. (1995). A major change with respect to Shetrone et al. (2015) is that the synthetic spectra were generated via TurboSpectrum (Alvarez & Plez 1998; Plez 2012), a local thermodynamic equilibrium (LTE) spectral synthesis code that can be used in both plane-parallel and spherical geometries. Turbospectrum version 15.2, the latest TurboSpectrum release at the time of these calculations, was used here. TurboSpectrum is also the code used to compute the synthetic spectral libraries for DR16 (Jönsson et al. 2020).

The LTE MARCS code (Gustafsson et al. 2008) was used to construct the stellar atmosphere models, spanning 56 depth points. For consistency, standard MARCS physical parameters were adopted: 1.5 for the mixing length parameter, 0.076 for the temperature distribution within the convective elements, and 8 for the energy dissipation by turbulent viscosity. The model atmosphere for the Sun was computed in plane-parallel geometry, while the model for Arcturus was computed in spherical geometry, assuming a mass of $0.7\,M_{\odot}$. The models were also computed with self-consistent chemical abundance distributions.

We use a microturbulent velocity of $0.7\,{\rm km\,s^{-1}}$ for the COD synthetic spectra of the Sun (e.g., Blackwell et al. 1995). The spectra were convolved via a Gaussian kernel, corresponding to $1.20\,{\rm km\,s^{-1}}$, which helps account for the instrumental profile. We adopt a microturbulent velocity of $1.7\,{\rm km\,s^{-1}}$ for Arcturus (Ramirez & Allende Prieto 2011). Synthetic spectra of Arcturus were convolved with a rotational profile for $v \sin i = 2\,{\rm km\,s^{-1}}$ (Gray 1981; Gray & Brown 2006), calculated with a limb-darkening parameter of 0.48 (Claret 2000), and with a Gaussian kernel of $\sigma = 1.9\,{\rm km\,s^{-1}}$ to correct the spectra for both rotational and resolution effects.

For the Sun, the abundances are taken from Grevesse et al. (2007). The abundances adopted for Arcturus were drawn from a small number of studies, with most being drawn from Ramirez & Allende Prieto (2011); the abundances adopted for

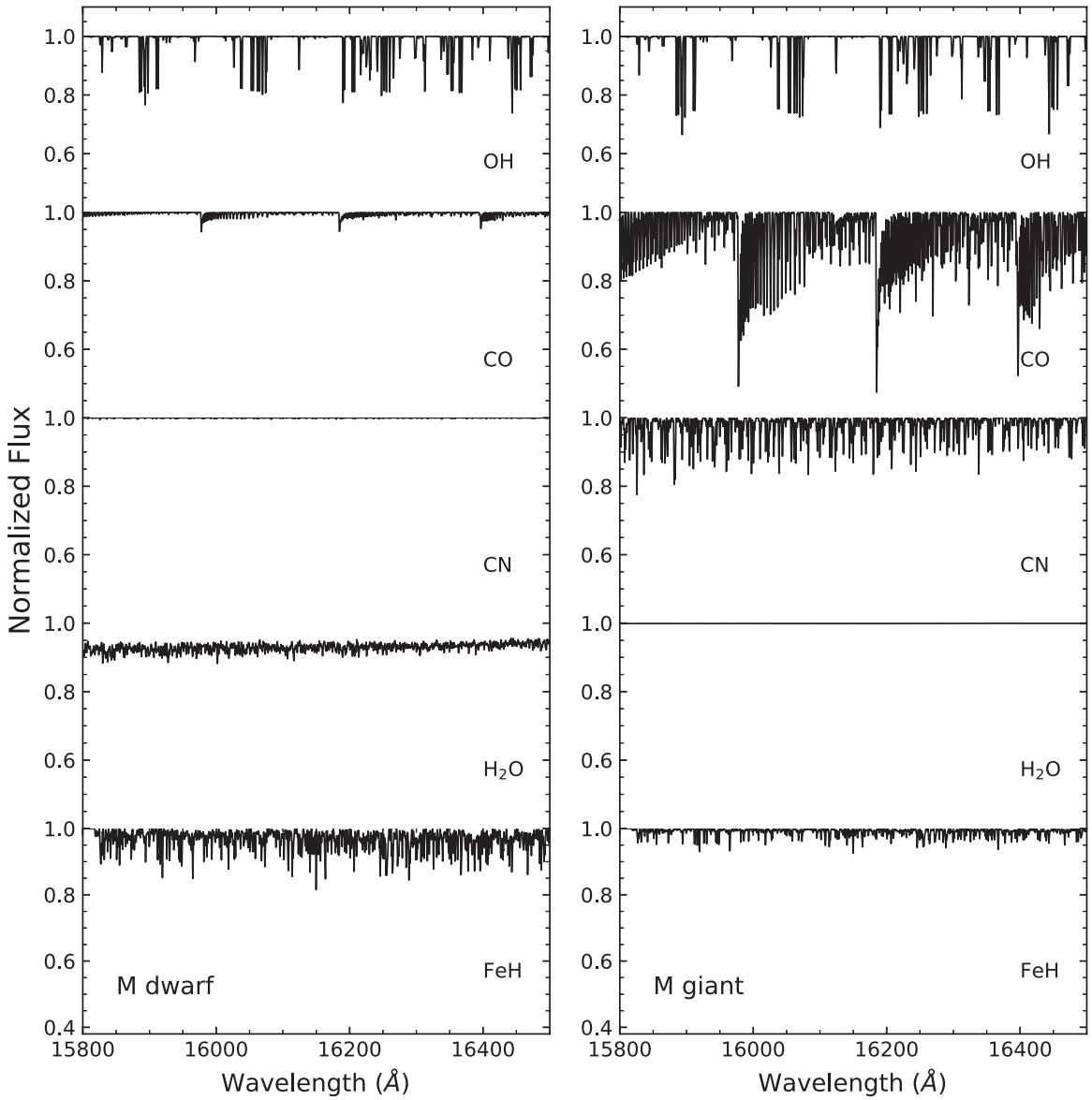

Figure 6. Illustration of absorption from the major molecular species (CO, OH, CN, H_2O, and FeH) in typical red giant ($T_{\rm eff} = 3800$ K, $\log g = 1.2$, $\xi = 2.0$ km s^{-1}, [Fe/H] =0.0) and M-dwarf ($T_{\rm eff} = 3500$ K, $\log g = 4.4$, $\xi = 1.0$ km s^{-1}, [Fe/H] = 0.0) spectra.

the Sun and Arcturus are summarized in Table 4. In addition to Ramirez & Allende Prieto (2011), the CNO abundances for Arcturus were derived here as part of the DR16 line list upgrade, using the same OH, CO, and CN lines as discussed Section 2.

The CNO abundances derived here for Arcturus can be compared to two recent detailed analyses of CNO in Arcturus, by Abia et al. (2012), and Sneden et al. (2014). Abia et al. (2012) analyzed the same FTS spectrum of Arcturus used here, but focused their analysis on the wavelengths λ4.55–5.56 μm, which also contains transitions of OH, CO, and CN. Differences in the CNO abundances derived here as compared to those of Abia et al. are small, with Δ = APOGEE—Abia et al. (2012) being $\Delta(A(^{12}{\rm C})) = -0.03$, $\Delta(A(^{14}{\rm N})) = -0.05$, and $\Delta(A(^{16}{\rm O})) = -0.13$. In both studies, the carbon isotope ratios are similar, with $^{12}{\rm C}/^{13}{\rm C} = 7 \pm 1$ derived here, and 9 ± 2 from Abia et al. (2012). A comparison with Sneden et al. (2014) is particularly interesting, as their analysis is based on the optical spectrum of Arcturus, with the carbon abundance determined using C_2 Swan bands at 4737 and 5135 Å, as well as the CH *G*-band around 4270–4330 Å, the nitrogen abundance from red CN lines in spectral intervals from λ6000–11000, and the oxygen abundance from the [O I] line at λ6300.27. The Arcturus CNO abundances derived here match well with those of Sneden et al. (2014), with $\Delta(A(^{12}{\rm C})) = +0.01$, $\Delta(A(^{14}{\rm N})) = -0.04$, and $\Delta(A(^{16}{\rm O})) = +0.01$. Sneden et al. (2014) also derive $^{12}{\rm C}/^{13}{\rm C} = 7 \pm 1$ from CN lines near λ8000. Taken together, these three independent determinations of CNO in Arcturus suggest that the abundances of these important elements are well-constrained for this standard red giant.

The compiled line list described in Section 2, covering the wavelength range from λ15000 to 17000, was used as input for the line-matching code. TurboSpectrum was used to generate spectra for individual atomic lines in the list, with a continuum line depth adopted so as to select spectral lines strong enough in either, or both, of the spectra of Arcturus and the Sun, for use in defining astrophysical adjustments. Given the different

Table 4
Adopted Elemental Abundances for the Sun and Arcturus

Z	Elem.	Sun	Arcturus	Reference
6	C	8.39	8.03	This study
7	N	7.78	7.62	This study
8	O	8.66	8.63	This study
11	Na	6.17	5.76	Ramirez & Allende Prieto (2011)
12	Mg	7.53	7.38	Ramirez & Allende Prieto (2011)
13	Al	6.37	6.19	Ramirez & Allende Prieto (2011)
14	Si	7.51	7.32	Ramirez & Allende Prieto (2011)
15	P	5.36	5.11	Maas et al. (2017)
16	S	7.14	6.94	Ryde et al. (2009)
19	K	5.08	4.76	Ramirez & Allende Prieto (2011)
20	Ca	6.31	5.90	Ramirez & Allende Prieto (2011)
21	Sc	3.05	2.84	Ramirez & Allende Prieto (2011)
22	Ti	4.90	4.65	Ramirez & Allende Prieto (2011)
23	V	4.00	3.54	Wood et al. (2014)
24	Cr	5.64	5.07	Ramirez & Allende Prieto (2011)
25	Mn	5.39	4.66	Ramirez & Allende Prieto (2011)
26	Fe	7.45	6.93	Ramirez & Allende Prieto (2011)
27	Co	4.92	4.49	Ramirez & Allende Prieto (2011)
28	Ni	6.23	5.77	Ramirez & Allende Prieto (2011)
29	Cu	4.21	3.71	Ramirez & Allende Prieto (2011)
58	Ce	1.58	0.99	Cunha et al. (2017)
60	Nd	1.45	0.94	Overbeek et al. (2016)
70	Yb	1.08	0.63	This study

quality of the reference spectra, lines deeper than 0.003 in the Sun, and 0.01 in Arcturus, were included as potential targets for astrophysical adjustments, if the uncertainties in the *gf*-values were known. We account for the reduced reliability of lines lacking known uncertainties and, in this case, keep only those lines deeper than 0.0075 and 0.025 for the Sun and Arcturus, respectively. The criteria described above result in a list of 1664 atomic lines, measured for astrophysical adjustments in relation to at least one of the standard stars. We also investigated 250 lines deeper than 0.15 of the continuum level in the solar spectrum for the purpose of damping constant adjustments (the shallower lines lack sufficient signal in their wings for this task).

The lines in the list were adjusted in order of their depth, starting with the deepest. For each line, a 0.8 Å wavelength range was considered, unless the line had HFS components. In the latter case, the wavelength range was extended by 0.4 Å beyond the bluest and reddest components of the HFS families. Parameters for the entire HFS family were changed simultaneously during the fitting. The line position was permitted to vary by up to 0.25 km s^{-1} (or up to 0.013 Å at 16000 Å), while the $\log(gf)$ value could vary by up to twice its estimated uncertainty in the course of the least-squares optimization, which utilized the downhill simplex algorithm (Nelder & Mead 1965). The spectra of the Sun and Arcturus were considered separately for each line of interest, and the resulting $\log(gf)$ value represents the weighted mean over both stars, where the weight is the line depth; this is the same method as that employed by Shetrone et al. (2015). The effects of strong line wings were taken into account by computing synthetic spectra over a wider range (±9 Å) before cutting out the smaller piece for fitting.

Some of the spectral lines that were adjusted had no known or estimated $\log(gf)$ uncertainties, and the astrophysical adjustments to these lines were constrained to within −2.0 and +0.75 dex from the original $\log(gf)$. Iterations on the damping parameters for the strong solar lines were restricted to ±0.4 dex changes, with a 3.0 Å wavelength range being considered around the lines of interest.

The iterative process for the line parameter adjustments includes using the resulting line list as the input for the next iteration. We run several iterations of the line parameter adjustments as follows: firstly, two $\log(gf)$ iterations were performed for the solar spectrum. Next, two damping constant iterations were performed on the strong solar lines. Six further $\log(gf)$ iterations, using both the Sun and Arcturus, were then completed. Although the evaluation of a single line does not require iterative adjustment, it is required for lines in blends. While most of the line parameter adjustments converge quickly, $\log(gf)$ values for some lines do not settle down even after a large number of iterations. This occurs when two strong lines are located near each other in terms of wavelength. We found 36 such lines, which continue to have large $\log(gf)$ adjustments after all iterations. In these cases, the original $\log(gf)$ values were replaced by averaged values over the second-to-sixth iterations, which was found to provide good final fits.

The procedure used to derive the astrophysical adjustments resulted in a significantly reduced difference between synthetic and observed spectra for both the Sun and Arcturus, based on this single iterated line list. Figure 7 shows these differences as a function of wavelength; each point represents the rms value between the synthetic and observed spectra over 20 Å chunks, with a synthesis step of 0.02 Å. The initial differences are shown in red, and the final interated differences are in blue; for both the Sun and Arcturus, the initial differences are significantly larger than the final differences, with the single interated line list providing superior fits to both standard stars. We note again that changes to the *gf*-values of the atomic lines are limited to values that are less than twice the uncertainties. In the case of the Sun, the mean rms value is 0.017 initially, and is reduced to 0.008 in the final line list, while for Arcturus, the corresponding mean rms values are 0.026 and 0.018, respectively. Overall fits are better for the Sun as compared to Arcturus, as the solar spectrum displays far fewer lines and much less spectral-line absorption than Arcturus (there are larger stretches of "line-free continuum" in the Sun). Overall in the APOGEE window, Arcturus has about 2.2 times greater absorption than the Sun (122 Å of equivalent-width absorption, in total, compared to 55 Å for the Sun).

Differences between the observed and the synthetic solar and Arcturus spectra generated by the final iterated line list were used to identify mismatched regions, which were then not used in fitting library spectra to observed spectra in ASPCAP. These mismatched regions were excluded from the fits to library spectra by use of a global mask, consisting of a weight of either 0.0 or 1.0 for each wavelength (pixel). Wavelengths were identified where the difference between the observed and synthesized spectra of Arcturus is greater than 0.05 in normalized flux, or where the difference between the observed and synthesized spectra of the Sun is greater than 0.03 in normalized flux; the pixels at these wavelengths were given zero weight in the fits, while the other pixels were assigned a weight equal to 1.0. The comparison was made using spectra smoothed to APOGEE resolution. Some regions masked by this algorithm were removed because they were considered to be residuals of telluric lines still present in the observed spectra. Following visual inspection, one mask, covering a region

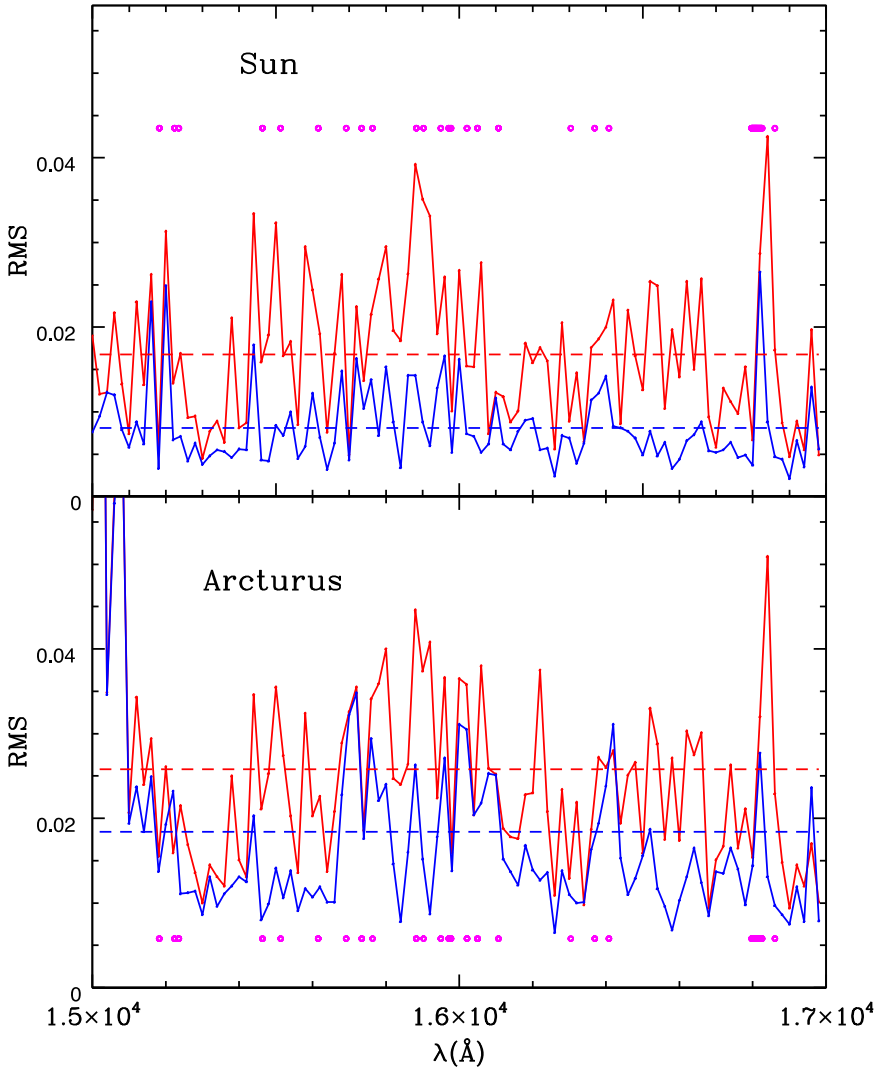

Figure 7. The rms difference between synthetic and observed spectra, calculated in 20 Å chunks, with the original (dashed line) and astrophysically adjusted (solid line) line lists for the Sun (upper panel) and Arcturus (lower panel). The dashed lines show the median rms for the whole spectrum with the adjusted line list. The small magenta circles in both panels indicate masked regions, where the final line list produces relative flux mismatches between synthetic and observed spectra of 0.03, or larger, for the Sun, and 0.05, or larger, for Arcturus. These masked pixels account for 3.3% of the APOGEE wavelength coverage.

λ16040–16050, was widened somewhat, and one covering the Brackett-11 hydrogen line at $\lambda 16806.5 \pm 15$ was added manually. This process resulted in 21 regions of the spectra being masked out in all DR16 ASPCAP-fits of both parameters and abundances. For completeness, the global mask wavelengths and weights are presented in Table 5. These 21 mask regions are indicated in both panels of Figure 7 by small magneta circles, and illustrate that the masked wavelengths account for only a tiny fraction (3.3%) of APOGEE pixels.

3.2. Astrophysical log(gf) Values

The differences between the original and final iterated $\log(gf)$ values, as $\Delta \log(gf)_{\text{(final – initial)}}$, are displayed as histograms in Figure 8 for a sample of 5 key chemical species (Fe I, Mg I, Al I, Si I, Ni I). In the middle panel dpicted as horizontal lines, we show the maximum amounts by which the $\log(gf)$ values were permitted to vary, depending on the estimated uncertainty in the *gf*-values themselves, using the NIST scale of A, B, C, D; recalling that the $\log(gf)$ values were permitted to vary by plus-or-minus twice their estimated

Table 5
Global Mask to Remove Regions of the Spectra not Fit Well by the Line-fitting Code for Arcturus or the Sun

Wavelength (Å, air)	Mask Value
15148.081	1.000
15148.290	1.000
15148.499	1.000
15148.709	1.000
15148.918	1.000
15149.127	1.000
15149.337	1.000
15149.546	1.000
15149.755	1.000
15149.965	1.000
…	…

Note. This is only an excerpt from the table, to show its form and content. The complete table is available in electronic form.

(This table is available in its entirety in machine-readable form.)

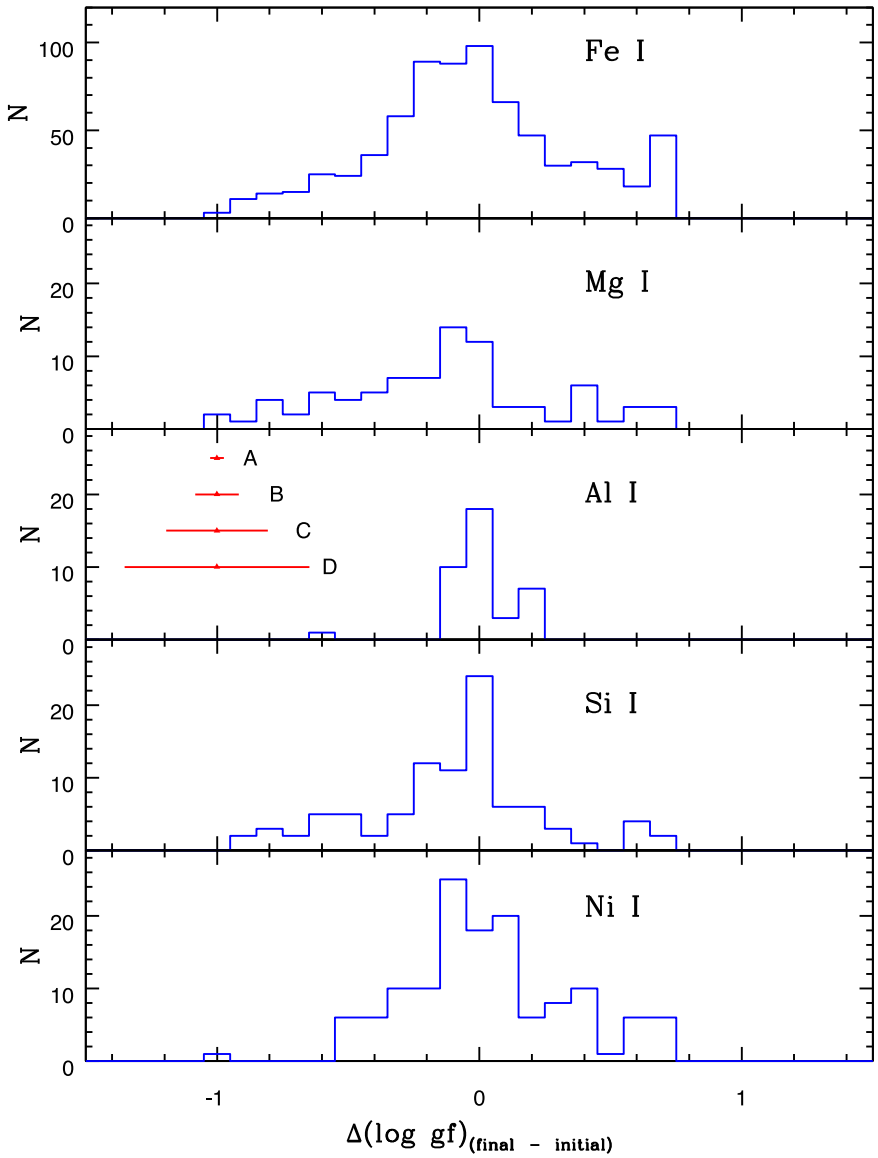

Figure 8. Distributions of the differences between the final astrophysically adjusted (iterated) and initial *gf*-values shown for five important species in the APOGEE spectra. No large systematic differences are found, in general, between the final and initial *gf*-values, with scatter peaked around differences of ∼0.0 dex. The larger differences (∼0.3 dex, or greater) between final and initial *gf*-values are found for weak lines (with no published uncertainties); these were not used for any ASPCAP abundance windows, and had negligible effects on the synthetic spectra.

uncertainty, it is these values that are illustrated by the horizontal lines. Overall, there are no significant systematics in the distributions of $\Delta\log(gf)$, with all of the elements scattering around zero. The largest differences relate, in general, to weaker lines with larger uncertainties in their *gf*-values (or unknown uncertainties); these are not used in the abundance windows in ASPCAP.

As an example of how the weaker atomic lines (which have a relatively small impact on derived abundances) have larger uncertainties in their *gf*-values, Figure 9 is used to illustrate the differences between final and initial *gf*-values for the key species, shown in Figure 8, as a function of relative line strength ($S = \log(gf\lambda) - \theta\chi$). The species illustrated in Figures 8 and 9 are not special in terms of their *gf*-values, so the results shown here are, in general, similar for other atomic elemental lines. This particular choice of elements spans a range of nucleosynthetic origins (Fe-peak, α-elements, and odd-Z), as well as atomic spectral characteristics. Lines used in abundance windows are plotted as large, filled red symbols, while those lines not used as abundance indicators are indicated by smaller open symbols. Note that for all elements shown, lines used to derive abundances are stronger lines (clearly detectable, with $S > -8$ or -9, depending on the element in question), and tend to have relatively well-defined *gf*-values (the differences between the final and initial *gf*-values are small). The weaker lines, where $S < -9.5$, exhibit significantly larger dispersion in their $\Delta\log(gf)$-values, were not used to constrain individual abundances, and did not have appreciable effects on abundance fits. Each panel notes the mean and standard deviations in the $\Delta\log(gf)$-values for the lines used in the abundance windows; it is found that all offsets are small ($\leqslant$0.1 dex), suggesting that APOGEE abundance offsets due to atomic line parameters are expected to be small.

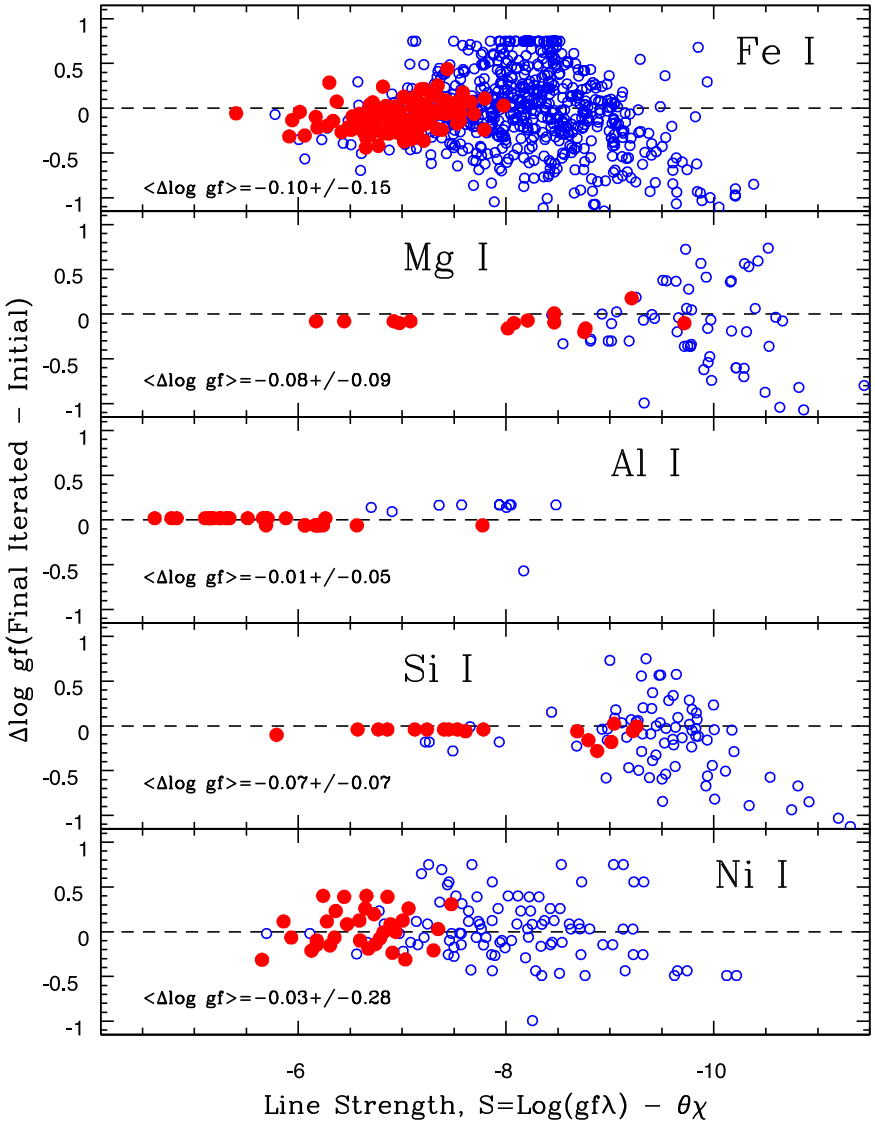

Figure 9. Differences between the final and initial log *gf*-values (Δlog gf) for the elemental lines from Figure 8 as a function of relative line strength. Lines used to measure individual chemical abundances are plotted as filled red symbols, with these transitions representing, primarily, the stronger lines for each species ($S > -8$ or -9), and having well-defined oscillator strengths, resulting in smaller iterative corrections. The weaker lines ($S < -9$), with larger uncertainties in their oscillator strengths, have little-to-no impact on derived abundances. Mean and standard deviations of the Δlog(*gf*)-values for lines used in abundance windows are shown for each species.

3.3. Astrophysical Damping Values

Differences between the original and iterated damping constants for Mg I, Al I, Si I, Fe I, and Ni I are shown in Figure 10; these differences were determined via fits to strong solar lines (not to Arcturus). There are systematic offsets in $\Delta(\log \Gamma)$ for both Fe I and Ni I, while there are no significant offsets for the Mg I and Si I damping constants. There is an offset of ~ -0.1 dex for Al I, although this is for only three lines, all of which arise from the same lower and upper spectroscopic configurations. In this spectral region, the Mg I and Si I lines are stronger than the Fe I and Ni I lines, which may explain why the differences between the initial and iterated damping constants display somewhat different behaviors. The stronger lines (Mg I and Si I) have more well-defined damping wings as compared to the weaker Fe I and Ni I lines in the Sun.

4. Discussion

4.1. Missing Lines and Significantly Mismatched Lines

In spite of the efforts made to add spectral lines, syntheses of both Arcturus and the Sun reveal a small number ($\sim$12) of observed, well-defined spectral lines with depths of 5%–25% that are seemingly missing from the DR16 line list. Not included in this discussion are lines with merely mismatched *gf*-values, as *gf*-values are adjusted (within limits) by fitting Arcturus and the Sun (COD) with weights determined by the relative line depths in the two standard stars; some lines do not fit as well as others in both stars simultaneously, but these lines are clearly present in both observed and model spectra. The true missing lines are presented in Table 5. The information tabulated includes the measured λ (in air), and the depth of the line in both Arcturus and the Sun (CoD), along with possible identifications from the DR16 line list, the NIST database, or from Hinkle et al. (1995). Seven of the missing lines have near-

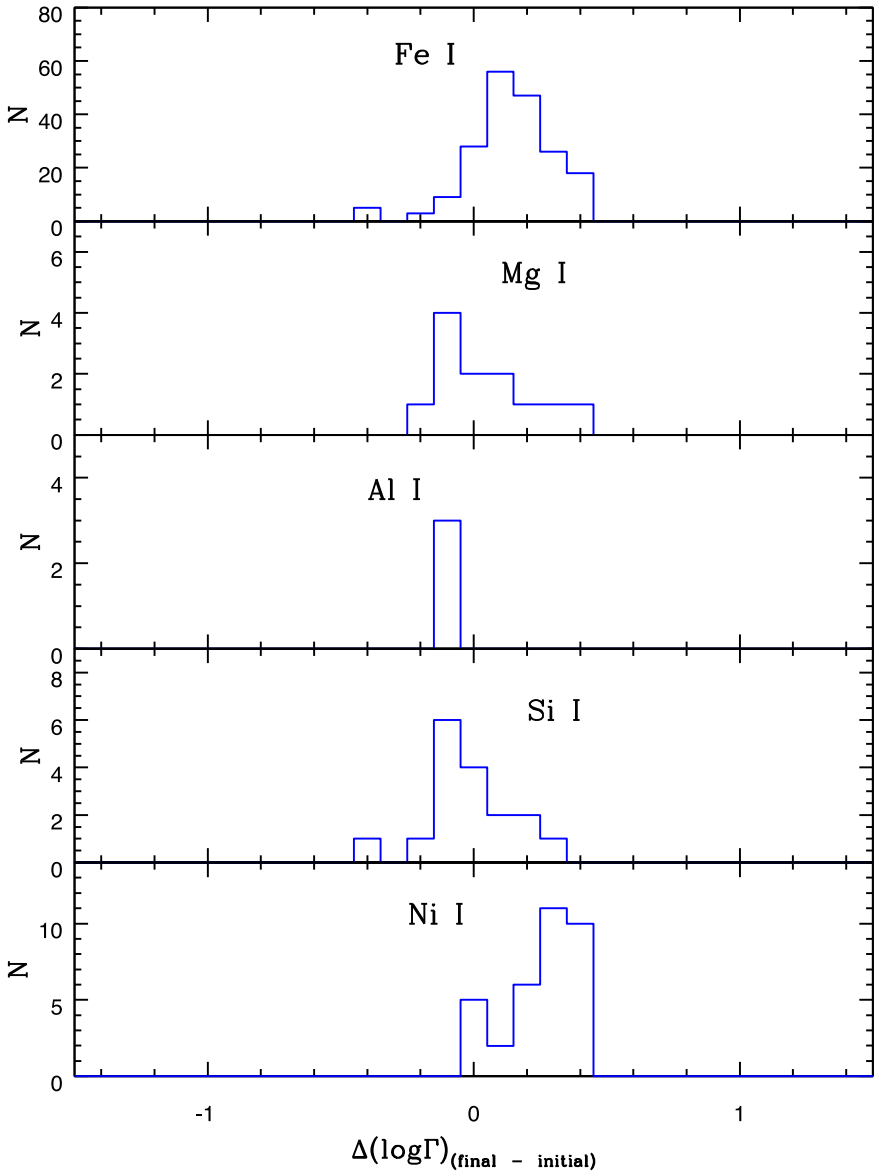

Figure 10. The difference between the astrophysically adjusted (new) and original (old) values of damping constants for lines from five of the major elemental species. In the APOGEE spectral window, the Mg I, Al I, and Si I lines are typically stronger than the Fe I and Ni I lines; it is worth noting that the $\Delta(\log\Gamma)$ values for Mg I and Si I scatter about zero (Al I, with only 3 lines, is not considered in this comparison), while the values for the (weaker) Fe I and Ni I lines are offset slightly to positive values.

wavelength matches with Fe I lines in the NIST database, with these lines being unclassified. It is likely that these seven "matches" are the unclassified, high-excitation Fe I lines tabulated in NIST.

An additional set of lines that are not well-fit either with the Sun or Arcturus consist of a small number of primarily high-excitation Fe I lines from the Kurucz line list. In some cases, the model lines are much too strong as compared to those of the Sun or Arcturus, such that the *gf*-values would need to be decreased by up to 3–4 in the log, and vice versa, where the model lines are orders-of-magnitude weaker than the observed line. R. L. Kurucz (2020, private communication) notes that the energy-level wave functions are linear combinations of basis states for the standard LS-coupling scheme, and large uncertainties can therefore occur in the *gf*-values for LS-forbidden lines, which can only arise by virtue of level mixing in these high-excitation energy levels. Carefully characterizing this sample of Fe I lines would be a useful future exercise. In addition, the missing broad feature near λ15967.18 is likely to be Co I (from the Kurucz line list, $\chi = 5.964$ eV), as the hfs components closely match the shape of the feature, although the *gf*-values would need to be increased by several orders of magnitude to fit the feature in both Arcturus and the Sun (presumably the same effect as discussed above for Fe I lines).

In both cases of missing lines, or seriously mismatched lines, the wavelength regions (which fall over very small pieces of the APOGEE wavelength space) are masked from fitting observed spectra to model spectra in ASPCAP (Jönsson et al. 2020). All of the missing lines in Table 6 are masked out, with the exception of that at $\lambda_{\rm Air}$15402.76 Å.

4.2. Evaluating the Utility of the DR16 Line List

The DR16 line list was created from a combination of data based on laboratory measurements, semi-empirical, and theoretical calculations from a wide range of sources. Atomic

Table 6
Missing Lines from the DR16 Line List and Possible Identifications

λ(Å)$_{air}$	α Boo Depth	Solar Depth	Possible ID: DR16 List	Possible ID: NIST	Hinkle et al. ID
15178.23	0.20	0.23	V I 78.26 Mn I 78.26	Fe I 78.25 uncls	
15402.76	0.06	0.06	Fe I $\log(gf) = -3.96$	⋯	bl OH (no)
15459.40	0.15	0.17	⋯	Fe I 59.31 uncls	⋯
15508.92	0.09	0.05	Sc I 508.92	⋯	⋯
15687.44	0.14	0.12	⋯	⋯	⋯
15729.75	0.21 (bl CN)	0.16	Fe I 29.81	Fe I 29.76	Fe I (probable)
15945.26	0.16	0.10	Mn I or Ti I ?	Fe I 45.26 uncls	Fe I
15967.18	0.17 (broad hfs?)	0.10 (broad hfs?)	Co I ∼67.18 (hfs)	⋯	CN (no)
15973.02	0.16 (broad sym)	0.11 (broad sym)	⋯	⋯	⋯
16016.75	0.19	0.13	Ni I or Zr I ?	Fe I 16.78 uncls	Fe I (probable)
16820.50	0.27	0.27	⋯	Fe I 20.52	Fe I (probable)
16855.73	0.12	0.08	Cr I 55.67	⋯	blend

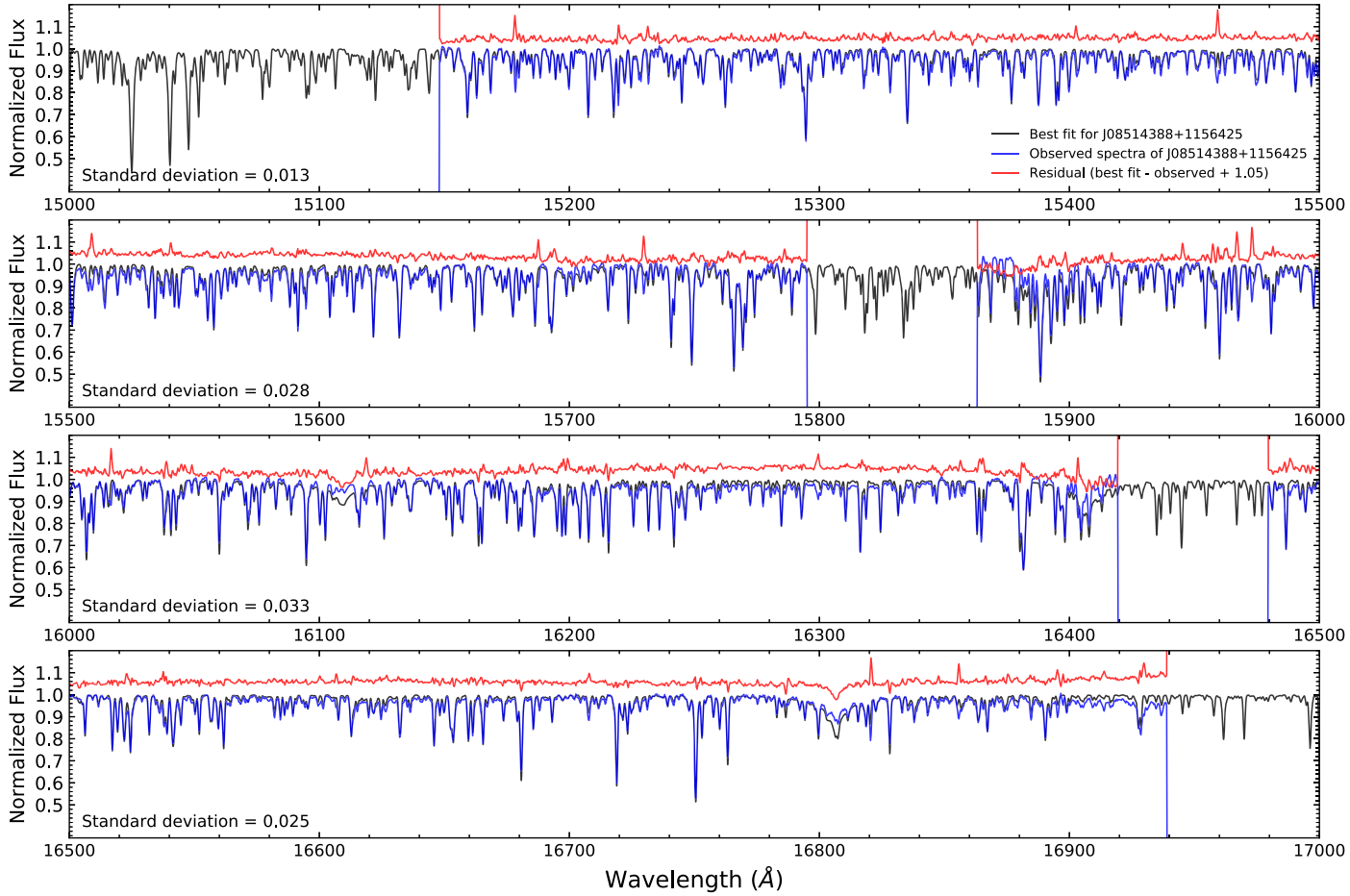

Figure 11. Synthetic spectrum computed with the DR16 line list for a red-clump star. The adopted stellar parameters are taken from Souto et al. (2018). The best-fit synthetic spectrum is shown in black, the observed in blue, and the difference between them shown by the (shifted) red line.

parameters, most importantly *gf*-values and damping constants, were adjusted, within limits defined by the accuracy of these values, by fitting with the Sun and Arcturus. It is worthwhile to employ this line list in a classical analysis of a star, and to compare the derived parameters and abundances with the relevant results from ASPCAP. Such an example comparison is presented here.

One relevant example is to apply such a classical analysis to the chemical analysis of a star in a well-studied open cluster, for which the metallicity and age are well-constrained. M67 is one such well-studied cluster, having a roughly solar metallicity and solar age. Souto et al. (2018, 2019) analyzed a large number of M67 members from different evolutionary states using APOGEE spectra, and found evidence of diffusion in this cluster.

We selected one star member of M67 from Souto et al. (2018), and computed the chemical abundances of several elements. The star is 2M08514388+1156425 ($T_{\rm eff} = 4820$ K, $\log g = 2.44$), which is a red-clump giant member of M67. The methodology adopted in the chemical abundance analysis, including the lines measured, is discussed in Souto et al. (2019) and the stellar parameters are adopted from Souto et al. (2018).

We note that in this case, unlike ASPCAP, we are not fitting the entire spectrum. A comparison of the synthetic spectrum with the observed APOGEE spectrum is shown in Figure 11.

There is an overall good fit for most of the spectrum, although in this case, the abundances were derived only for selected lines (see Souto et al. for details). The abundances obtained are all within the expected range for a star member of M67, including a recovered iron abundance of $A(\mathrm{Fe}) = 7.48$, which is close to the solar abundance adopted in the construction of the line list and the adjustment of the *gf*-values. A comparison of 13 abundances, derived classically with ASPCAP values from DR16 finds, based on the elements Fe, C, N, O, Na, Mg, Al, Si, K, Ca, Ti, V, and Mn, a mean difference and standard deviation of $\Delta[\mathrm{X/H}] = +0.04 \pm 0.05$ dex. This comparison suggests that the DR16 line list can be used as a general quantitative spectroscopy tool for both red giants and cool main-sequence stars.

V.S. and K.C. acknowledge that their work here is supported, in part, by the National Aeronautics and Space Administration under grant 16-XRP16-2-0004, issued through the Astrophysics Division of the Science Mission Directorate, as well as the NSF grant AST-2009507. T.M. and D.A.G.H. acknowledge support from the State Research Agency (AEI) of the Spanish Ministry of Science, Innovation and Universities (MCIU), and the European Regional Development Fund (FEDER), under grant AYA2017-88254-P. J.H. and D.B. acknowledge support from NSF grant AST-1715898. S.M. has been supported by the János Bolyai Research Scholarship of the Hungarian Academy of Sciences, by the Hungarian NKFI Grants K-119517 and GINOP-2.3.2-15-2016-00003 of the Hungarian National Research, Development and Innovation Office, and by the ÚNKP-20-5 New National Excellence Program of the Ministry for Innovation and Technology.

We would like to thank the anonymous referee for a careful reading of the initially submitted manuscript, and very constructive comments and questions, which improved the final version of this paper.

SDSS-IV is managed by the Astrophysical Research Consortium for the Participating Institutions of the SDSS Collaboration, including the Brazilian Participation Group, the Carnegie Institution for Science, Carnegie Mellon University, the Chilean Participation Group, the French Participation Group, the Harvard-Smithsonian Center for Astrophysics, Instituto de Astrofísica de Canarias, The Johns Hopkins University, Kavli Institute for the Physics and Mathematics of the Universe (IPMU)/University of Tokyo, Lawrence Berkeley National Laboratory, Leibniz Institut für Astrophysik Potsdam (AIP), Max-Planck-Institut für Astronomie (MPIA Heidelberg), Max-Planck-Institut für Astrophysik (MPA Garching), Max-Planck-Institut für Extraterrestrische Physik (MPE), National Astronomical Observatory of China, New Mexico State University, New York University, University of Notre Dame, Observatrio Nacional/MCTI, The Ohio State University, Pennsylvania State University, Shanghai Astronomical Observatory, United Kingdom Participation Group, Universidad Nacional Autónoma de México, University of Arizona, University of Colorado Boulder, University of Oxford, University of Portsmouth, University of Utah, University of Virginia, University of Washington, University of Wisconsin, Vanderbilt University, and Yale University.

ORCID iDs

Verne V. Smith https://orcid.org/0000-0002-0134-2024
Dmitry Bizyaev https://orcid.org/0000-0002-3601-133X
Katia Cunha https://orcid.org/0000-0001-6476-0576
Matthew D. Shetrone https://orcid.org/0000-0003-0509-2656
Diogo Souto https://orcid.org/0000-0002-7883-5425
Carlos Allende Prieto https://orcid.org/0000-0002-0084-572X
Thomas Masseron https://orcid.org/0000-0002-6939-0831
Henrik Jönsson https://orcid.org/0000-0002-4912-8609
Sten Hasselquist https://orcid.org/0000-0001-5388-0994
Yeisson Osorio https://orcid.org/0000-0001-5832-6933
D. A. García-Hernández https://orcid.org/0000-0002-1693-2721
Bertrand Plez https://orcid.org/0000-0002-0398-4434
Rachael L. Beaton https://orcid.org/0000-0002-1691-8217
Jon Holtzman https://orcid.org/0000-0002-9771-9622
Steven R. Majewski https://orcid.org/0000-0003-2025-3147
Guy S. Stringfellow https://orcid.org/0000-0003-1479-3059
Jennifer Sobeck https://orcid.org/0000-0002-4989-0353

References

Abia, C., Palmerini, S., Busso, M., & Cristallo, S. 2012, A&A, 548A, 55
Ahumada, R., Allende Prieto, C., Almeida, A., et al. 2019, ApJS, 249, 3
Alvarez, R., & Plez, B. 1998, A&A, 330, 1109
Asplund, M., Grevesse, N., & Sauval, A. J. 2009, ARA&A, 47, 481
Barber, R. J., Tennyson, J., Harris, G. J., & Tolchenov, R. N. 2006, MNRAS, 368, 1087
Biémont, E., Dutrieux, J.-F., Martin, I., & Quinet, P. 1998, JPhB, 31, 3321
Biémont, E., Martin, F., Quinet, P., & Zeippen, C. J. 1994, A&A, 283, 339
Biémont, E., Palmeri, P., & Quinet, P. 1999, Ap&SS, 269, 635
Bizyaev, & Shetrone 2015, AstroLines: Astrophysical line list generator in the H-band , Astrophysics Source Code Library, ascl:1502.022
Blackwell, D. E., Smith, G., & Lynas-Gray, A. E. 1995, A&A, 303, 575
Blackwell-Whitehead, R. J., Lundberg, H., Nave, G., Pickering, J. C., Jones, H. R. A., Lyubchik, Y., Pavlenko, Y. V., & Viti, S. 2006, MNRAS, 373, 1603
Blackwell-Whitehead, R. J., Xu, H. L., Pickering, J. C., Nave, G., & Lundberg, H. 2005, MNRAS, 361, 1281
Blanton, M. R., Bershady, M. A., Abolfathi, B., et al. 2017, AJ, 154, 28
Bowen, I. S., & Vaughan, A. H., Jr. 1973, ApOpt, 12, 1430
Brooke, J. S. A., Bernath, P. F., Western, C. M., Sneden, C., Afsar, M., Li, G., & Gordon, I. E. 2016, JQSRT, 168, 142
Burris, D. L., Pilachowski, C. A., Armandroff, T. E., Sneden, C., Cowan, J. J., & Roe, H. 2000, ApJ, 544, 302
Butler, K., C. Mendoza, C., & Zeippen, C. J. 1993, JPhB, 26, 4409
Claret, A. 2000, A&A, 363, 1081
Cunha, K., Smith, V. V., Hasselquist, S., et al. 2017, ApJ, 844, 145
Eisenstein, D. J., Weinberg, D. H., Agol, E., et al. 2011, AJ, 142, 72
Froese Fischer, C. 2002, The MCHF/MCDHF Collection (non-orthogonal B-spline CI caclulations) http://nlte.nist.gov/MCHF/
Fuhr, J. R., & Wiese, W. L. 2006, JPCRD, 35, 1669
García Pérez, A. E., Allende Prieto, C., Holtzman, J. A., et al. 2016, AJ, 151, 144
Goldman, A., Shoenfeld, W. G., Goorvitch, D., et al. 1998, JQSRT, 59, 453
Goorvitch, D. 1994, ApJS, 95, 535
Gray, D. F. 1981, ApJ, 245, 992
Gray, D. F., & Brown, K. I. 2006, PASP, 118, 1112
Grevesse, N., Asplund, M., & Sauval, A. J. 2007, SSRv, 130, 105
Gunn, J. E., Siegmund, W. A., Mannery, E. J., et al. 2006, AJ, 131, 2332
Gustafsson, B., Edvardsson, B., Eriksson, K., Jorgensen, U. G., Nordlund, A., & Plez, B. 2008, A&A, 486, 951
Hansen, J. E., Laughlin, C., van der Hart, H. W., Verbockhaven, G., et al. 1999, JPhB, 32, 2099
Hargreaves, R. J., Hinkle, K. H., Bauschlicher, C. W., Wende, S., Seifahrt, A., & Bernath, P. F. 2010, AJ, 140, 919
Hasselquist, S., Shetrone, M., Cunha, K., et al. 2016, ApJ, 833, 81

Hibbert, A., Biémont, E., Godefroid, M., & Vaeck, N. 1993, A&AS, 99, 179
Hinkle, K., Wallace, L., & Livingston, W. D. 1995, PASP, 107, 1042
Holtzman, J. A., Harrison, T. E., & Coughlin, J. L. 2010, AdAst, 2010, 193086
Jönsson, H., Holtzman, J. A., Allende Prieto, C., Cunha, K., García-Hernández, D. A., et al. 2020, AJ, 160, 120
Korotin, S. A. 2020, AstL, 46, 541
Kramida, A., Ralchenko, Yu., Reader, J. & NIST ASD Team 2017, NIST Atomic Spectra Database (ver. 5.7.1) https://physics.nist.gov/asd
Kurucz, R. L. 2017, Linelists: gfnew (gfallwn08oct17) http://kurucz.harvard.edu/linelists/gfnew/gfallwn08oct17.dat
Larsson, M. 1983, A&A, 128, 291
Lawler, J. E., Guzman, A., Wood, M. P., Sneden, C., & Cowan, J. J. 2013, ApJS, 205, 11
Li, G., Gordon, I. E., Rothman, L. S., et al. 2015, ApJS, 216, 15
Livingston, W., & Wallace, L. 1991, An Atlas of the Solar Spectrum in the Infrared from 1850 to 9000 cm^{-1} (1.1 to 5.4 microns), NSO Tech. Rep.
Maas, Z. G., Pilachowski, C. A., & Cescutti, G. 2017, ApJ, 841, 108
Majewski, S. R., Schiavon, R. P., Frinchaboy, P. M., et al. 2017, AJ, 154, 94
Mendoza, C., Eissner, W., Le Dourneuf, M., & Zeippen, C. J. 1995, JPhB, 28, 3485
Nahar, S. N., & Pradhan, A. K. 1993, JPhB, 26, 1109
Nelder, J. A., & Mead, R. 1965, CompJ, 7, 308
Nidever, D. L., Holtzman, J. A., Allende Prieto, C., et al. 2015, AJ, 150, 173
Outred, M. 1978, JPCRD, 7, 1
Overbeek, J. C., Friel, E. D., & Jacobson, H. R. 2016, ApJ, 824, 75
Pehlivan Rhodin, A. 2018, PhD thesis, Lund Univ.
Pehlivan Rhodin, A., Hartman, H., Nilsson, H., & Jönsson, P. 2017, A&A, 598, 102
Piskunov, N. E., Kupka, F., Ryabchikova, T. A., Weiss, W. W., & Jeffrey, C. S. 1995, A&AS, 112, 525
Plez, B. 2012, Turbospectrum: Code for Spectral Synthesis, version 15.1, Astrophysics Source Code Library, ascl:1205.004
Polyansky, O. L., Kyuberis, A. A, Zobov, N. F, et al. 2018, MNRAS, 480, 2597
Ramirez, I., & Allende Prieto, C. 2011, ApJ, 743, 135
Ruffoni, M. P., Allende Prieto, C., Nave, G., & Pickering, J. C. 2013, ApJ, 779, 17
Ryabchikova, T., Piskunov, N., Kurucz, R. L., et al. 2015, PhyS, 90, 054005
Ryde, N., Edvardsson, B., Gustafsson, B., et al. 2009, A&A, 496, 701
Safronova, M. S., Safronova, U. I., & Clark, C. W. 2013, PhRvA, 87, 052504
Sansonetti, J. E. 2008, JPCRD, 35, 301
Shetrone, M., Bizyaev, D., Lawler, J. E., Allende Prieto, C., et al. 2015, ApJS, 221, 24
Šimečková, M., Jacquemart, D., Rothman, L. S., Gamache, R.R., & Goldman, A. 2006, JQSRT, 98, 130
Sneden, C., Lucatello, S., Ram, S. R., Brooke, J. S. A., & Bernath, P. 2014, ApJS, 214, 26
Souto, D., Cunha, K., García-Hernández, D. A., et al. 2017, ApJ, 835, 239
Souto, D., Cunha, K., Smith, V. V., et al. 2020, ApJ, 890, 133
Souto, D., Prieto, C. A., & Cunha, K. 2019, ApJ, 874, 97
Souto, D., Unterborn, C. T., Smith, V. V., et al. 2018, ApJL, 860, L15
Wallace, L., & Hinkle, K. 2001, ApJ, 559, 424
Wilson, J. C., Hearty, F. R., Skrutskie, M. F., et al. 2019, PASP, 131, 5001
Wood, M. P., Lawler, J. E., & Shetrone, M. 2014, ApJS, 787, 16
Yurchenko, S. N., Sinden, F., Lodi, L., et al. 2018a, MNRAS, 473, 5324
Yurchenko, S. N., Szabo, I., Pyatenko, E., & Tennyson, J. 2018b, MNRAS, 480, 3395
Zasowski, G., Cohen, R. E., Chojnowski, S. D., et al. 2017, AJ, 154, 198
Zasowski, G., Johnson, J. A., Frinchaboy, P. M., et al. 2013, AJ, 146, 81
Zatsarinny, O., & Bartschat, K. 2006, JPhB, 39, 2861